Impact of Air Hole Geometry on the Performance of InGaN/GaN Photonic Crystal Surface-Emitting Lasers

Wen-Hsuan Hsieh, Kuo-Bin Hong, Ching-Han Lin, Chen-Yu Yang, Tien-Chang Lu, *Senior Member, IEEE*, and Chia-Yen Huang, *Associate Member, IEEE*

***Abstract*—In this study, we demonstrate GaN-based photonic crystal surface-emitting lasers (PCSELs) employing two distinct air hole geometries: circular (CC) and right-isosceles-triangle (RIT). By systematically tuning the fill factor (FF) and lattice constant, the lasing wavelengths are maintained between 420–425 nm, enabling direct comparison of device performance. Optical simulations and experimental results confirm that the CC structure, characterized by high in-plane symmetry (C_{4v} group), supports degenerate Bloch modes at the Γ point, resulting in strong lateral confinement, low vertical radiation loss, and high Q-factors. These features enable low-threshold lasing. In contrast, the RIT structure intentionally breaks the in-plane rotational symmetry, lifting mode degeneracy via geometric asymmetry. This mode splitting selectively enhances the vertical radiation coupling of the desired B-mode while suppressing competing modes, facilitating stable single-mode operation. Although the RIT design yields a higher threshold due to the increased vertical loss, it also demonstrates superior slope efficiency beyond the threshold. The declining threshold trend with increasing FF in both configurations matches the simulated predictions.**

***Index Terms*—Photonic crystal, PCSEL, semiconductor laser, GaN, InGaN.**

I. Introduction

PHOTONIC crystal surface-emitting laser (PCSEL) has emerged as a promising light source for applications requiring high output power and low beam divergence, particularly in LiDAR [1], [2], advanced manufacturing [3], [4], [5], [6], and optical communication systems [7], [8], [9], [10]. In the near-infrared spectral region, III-arsenide-based PCSELs have demonstrated exceptional performance due to their ability to form lateral optical cavities via band-edge modes near the Γ point of the photonic crystal (PhC) band structure, simultaneously enabling vertical surface emission without external mirrors [11], [12], [13], [14], [15]. The lateral optical feedback originates from the slow-light characteristics and in-plane distributed feedback provided by the periodic refractive index profile at Bragg's condition, resulting in a high-quality factor (Q-factor) and single-mode lasing over a large area. [16], [17], [18]. Integration with wide-bandgap III-nitride materials is essential to extend PCSEL technology into the ultraviolet to visible spectrum [19], [20], [21]. However, realizing high-performance GaN-based PCSELs remains challenging due to intrinsic material and fabrication issues. The epitaxial growth of high-quality InGaN/GaN films is challenging due to the lattice mismatches and differences in thermal expansion coefficients with non-native substrates. Overgrowth behavior on nano-patterned GaN templates varied from platform to platform, which makes the fabrication of designated air hole arrays in GaN still challenging [22], [23], [24]. Liu et al. proposed to couple the InGaN active region with the externally deposited TiO_2 PhC waveguide as a compromised approach. However, electrical pumping became more critical due to the lack of a conductive TiO_2 [25], [26].

Despite these challenges, significant progress has been made in realizing GaN PCSEL. Matsubara et al. first demonstrated PCSEL operation in the blue-violet range using an InGaN/GaN structure with air holes embedded in the n-side of separate confinement heterostructures (SCH) via overgrowth techniques [27]. The threshold and the slope after lasing are modest at the beginning, but they are significantly improved later by the optimization in the lattice type and processing technologies by Emoto et al. [28]. Kawashima et al. located the PhC to the p-side of the waveguide by top-down dry-etching techniques [29]. Taguchi et al. extended the lasing wavelength into the green spectral range using a dual-lattice design and SiO_2-filled holes for improved structural stability [30]. Most of these studies have focused on the effects of air hole arrangement on the lasing performance. Although several studies have investigated the effects of air-hole shape and filling factor on the band structure and coupling coefficients in GaAs systems [31], [32], [33], systematic investigations in the III-nitride material platforms remain limited. In the III-nitride materials system, the alloy composition contrast in the laser waveguides is much limited due to the epitaxial strain, which also leads to a smaller refractive index contrast than that in the III-arsenide PCSELs. Therefore, a systematic study based on a practical III-nitride laser waveguide structure is strongly desired. In this study, we

Received 24 August 2025; revised 28 November 2025 and 20 December 2025; accepted 23 December 2025. Date of publication 31 December 2025; date of current version 16 January 2026. This work was supported by the National Science and Technology Council (NTSC) of Taiwan under Contract NTSC-113-2628-E-A49-008 and Contract NTSC 114-2923-E-A49-015-MY2. *(Corresponding author: Chia-Yen Huang.)*

Wen-Hsuan Hsieh, Ching-Han Lin, Chen-Yu Yang, Tien-Chang Lu, and Chia-Yen Huang are with the Department of Photonics and Institute of Electro-Optical Engineering, College of Electrical and Computer Engineering, National Yang Ming Chiao Tung University, Hsinchu 30010, Taiwan (e-mail: cyhuang06@nycu.edu.tw).

Kuo-Bin Hong is with Semiconductor Research Center, Hon Hai Research Institute, Taipei City 23678, Taiwan.

Color versions of one or more figures in this article are available at https://doi.org/10.1109/JSTQE.2025.3650007.

Digital Object Identifier 10.1109/JSTQE.2025.3650007

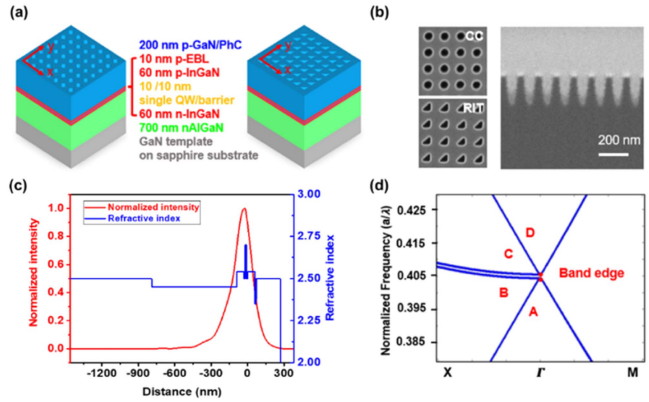

Fig. 1. (a). Schematic of GaN PCSEL structures with CC and RIT air holes. (b) SEM top-view image (left) of CC and RIT air holes. The cross-sectional view image of the CC hole is at the right. (c) Simulated normalized electric field intensity and refractive index profile along the epilayer direction. (d) Photonic band structure for a lattice period $a = 170$ nm and filling factor FF $= 10\%$.

introduced symmetric circular (CC) holes and asymmetric right isosceles triangle (RIT) holes to compare their threshold levels and output efficiencies due to the breaking of the odd symmetry of the electric field mode profile. The impact of the airhole filling factor (FF) on the laser performance of both hole geometries will be studied theoretically and experimentally. Through numerical simulations and experimental validation, we aim to establish robust design rules that guide the engineering of high-power, short-wavelength PCSELs based on III-nitride platforms.

II. Result and Discussion

Fig. 1(a) shows the three-dimensional schematic of GaN PCSELs featuring CC and RIT air holes. The airholes are patterned and etched from the surface of the device, enabling a more straightforward fabrication and higher reproducibility. The device structure comprises, from top to bottom: a 200 nm p-GaN layer with embedded airholes as the PhC layer, a 10 nm p-AlGaN electron blocking layer (EBL), a 60 nm p-$In_{0.03}Ga_{0.97}N$ waveguide layer, a 10 nm single quantum well (QW), a 60 nm n-$In_{0.03}Ga_{0.97}N$ waveguide layer, a 700 nm n-$Al_{0.05}Ga_{0.95}N$ layer, and a u-GaN template on a flat sapphire substrate. Fig. 1(b) shows the scanning electron microscope (SEM) images of the fabricated devices from the top-view and cross-sectional views. The left sub-images demonstrate uniform CC and RIT air holes in a square lattice, with a lattice period of a = 170 nm and a FF of 11%. The right sub-figure displays a vertical cross-sectional view of airholes, indicating an etch depth of approximately 200 nm, which agrees with our design. The sidewall is still $\sim 6°$ from vertical due to processing limitations. To avoid the etching to the EBL layer, dummy GaN wafers are coloaded to calibrate the etching rate prior to the etching on the laser epi. Fig. 1(c) shows the simulated electric field intensity ($|E|^2$) and refractive index distribution across the epilayers. The results indicate that the lasing mode is well-confined within the SCH and is coupled with the PhC slab. The confinement factor with the active region (Γ_{QW}) and the mode overlapping with the PhC (Γ_{PhC}) was estimated to be 4% and 9%, respectively. Fig. 1(d) shows the calculated photonic band diagram, based on the effective index method originally proposed in 2002 [34]. The effective permittivity of the air hole region, ε_a, and that of the background region, ε_b, are extracted by considering the limited vertical confinement of the optical mode. These values are calculated based on two constraints: the weighted average dielectric constant matches the square of the effective index (n_{eff}), and the dielectric contrast is scaled by the Γ_{PhC}. The expressions are in equation (1) and (2):

$$\varepsilon_a = n_{eff}^2 - (1 - FF) \cdot \Gamma_{PhC} \cdot (n_{GaN}^2 - n_{air}^2) \quad (1)$$

$$\varepsilon_b = n_{eff}^2 + FF \cdot \Gamma_{PhC} \cdot (n_{GaN}^2 - n_{air}^2) \quad (2)$$

This approximation compensates for the limited field penetration into the 2D PhC and allows a more accurate modeling of the in-plane photonic band of PCSELs. The band diagram reveals four distinct modes (A, B, C, D) near the Γ point with FF $= 10\%$. The normalized frequency (a/λ) of band edges is $\sim$0.404, where "a" is the lattice constant of PhC. Thus, for a target $\lambda = 420$ nm lasing, the lattice periodicity shall be around 170 nm, and the CC hole diameter and the width of RIT triangle is around 60 nm and 76 nm, respectively, for a 10% FF.

Three-dimensional finite-element method is employed to simulate the complex eigenfrequency ($\tilde{\omega}$) and electric-field distribution, $\mathbf{E}(\mathbf{r})$, of the band-edge modes of the input PCSEL structures by COMSOL Multiphysics. The PhC layer is assumed to be infinitely periodic in the lateral direction. The Q-factor (Q) of the primary modes A and B were calculated via the ratio of the real part (ω_r) and the imaginary part of $\tilde{\omega}$. The vertical radiation loss (α_{rad}) is then calculated by the following (3) and (4):

$$\alpha_{rad} = n_{av}\, \omega_r / (c \cdot Q) \quad (3)$$

$$n_{av} = \int \left(n(r) \cdot |\mathbf{E}(\mathbf{r})|^2 \right) dV / \int |\mathbf{E}(\mathbf{r})|^2 dV \quad (4)$$

where c and n(r) denote the speed of light and the refractive index profile. Γ_{QW} and Γ_{PhC} is estimated by the ratio of $\int |\mathbf{E}(\mathbf{r})|^2 dV$ in the quantum wells and PhC to that of all layers, respectively. Fig. 2(a) and (d) present the dependence of Γ_{QW} and Γ_{PhC} on the FF for both CC and RIT hole geometries, respectively. While Γ_{QW} shows minimal variation ($\sim$4%) across FF from 0.1 to 0.3 in both structures, Γ_{PhC} strongly depends on the FF. Γ_{PhC} declines with FF significantly due to the reduced overlapping of the optical mode with the PhC slab. This observation is consistent with the Q-factor results in Fig. 2(b) and (e). When the FF increases, the average refractive index of PhC is lowered, as in (1), which also enhances the penetration of the optical mode profile toward the substrate. As a result, more optical power is out-coupled from the substrate end. The Q-factor reduces accordingly with a higher FF. The dependence of the vertical radiation loss α_{rad} on the FF is shown in Fig. 2(c), where a larger α_{rad} enhances vertical out-coupling and slope efficiency at the expense of a reduced Q-factor and higher threshold. The Γ-point radiation loss is evaluated using the symmetry-consistent formulation $\alpha_{rad} = (2\pi/a)/Q$, under which CC structures exhibit vanishing vertical radiation in perfectly symmetric unit cells, consistent with Γ-point BIC theory, while

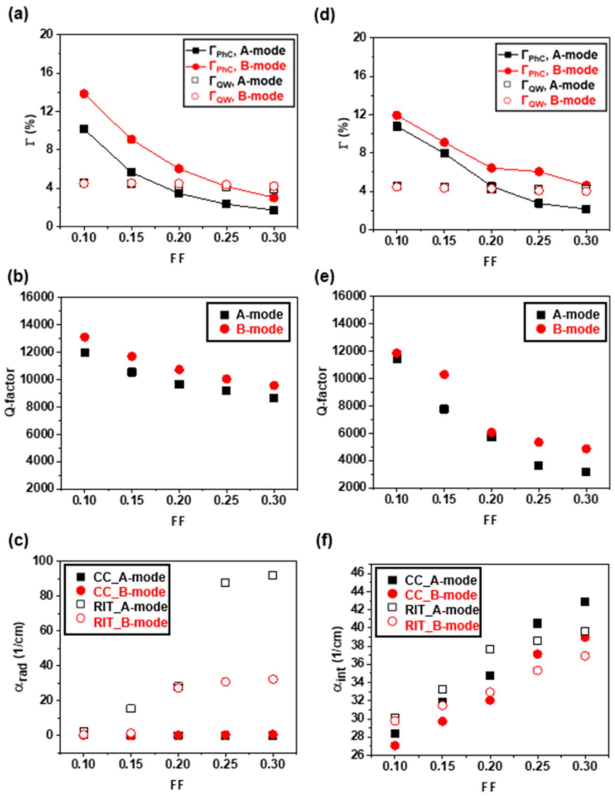

Fig. 2. The dependence of simulated Γ_{PhC} and Γ_{QW} of A-mode and B-mode on FF for PCSELs with (a) CC and (d) RIT holes. The dependence of Q-factors on FF for PCSELs with (b) CC and (e) RIT holes. The dependence of α_{rad} on FF for PCSELs with (c) CC and RIT holes. The dependence of α_{int} on FF for PCSELs with (f) CC and RIT holes.

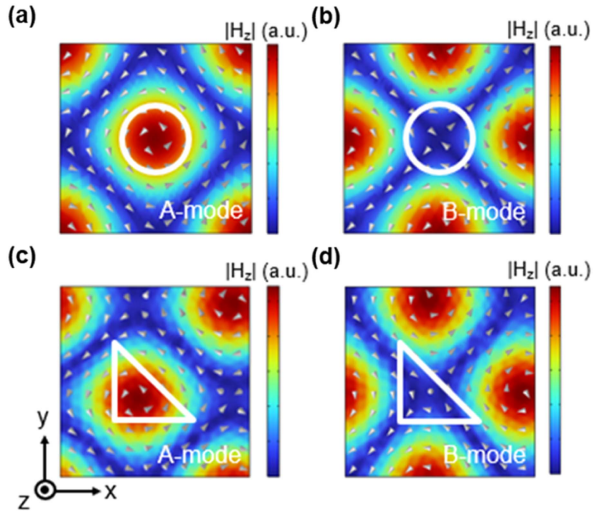

Fig. 3. Simulated in-plane electric field vectors (arrows) and magnetic field amplitude $|H_z|$ (color map) at the center of the photonic crystal layer with a lattice period a = 170 nm and fill factor FF = 0.1. (a), (b) show A-mode and B-mode field distributions for CC holes, while (c), (d) show those for RIT holes.

the internal loss $\alpha_{\mathrm{int}} = 2\pi \mathrm{f}/\mathrm{Q}_{\mathrm{factor}}$ is evaluated independently in Fig. 2(f). Regardless of hole geometry and FF, the B-mode consistently shows higher Γ_{PhC} and Q-factor, confirming it as the dominant lasing mode in both CC and RIT structures [31], [32].

It's worth noticing that a PCSEL with CC holes exhibits a higher Q-factor and a lower α_{rad} than that with RIT holes when FF>10%, which is attributed to the high symmetry of CC air-holes. Fig. 3 shows the in-plane electric vector field distribution in arrows and the absolute z-component of the magnetic field (H_z) in color mapping in the middle of the PhC layer. The thick white line illustrates the perimeter of the air hole. In Fig. 3(a) and (b), the electric field distribution shows an inverse odd symmetry, i.e., $\vec{\mathrm{E}}(-\mathrm{x}, -\mathrm{y}) = -\vec{\mathrm{E}}(\mathrm{x}, \mathrm{y})$. The radiation strength is governed by the phase difference between vertically diffracted waves generated by counter-propagating in-plane fundamental modes. For PCSEL with a square lattice, the two counter-propagating waves along the x or y directions are inherently out of phase at Bragg's condition, resulting in a π phase difference between their diffracted components with the inverse coordinates. CC holes exhibit even symmetry in all directions, resulting in complete destructive interference and suppression of vertical radiation. In contrast, the even symmetry of RIT holes is broken along the $\hat{x} + \hat{y}$ direction, as shown in Fig. 3(c) and (d). The hole asymmetry produces partial constructive interference and thus an enhanced vertical radiation. Therefore, the α_{rad} is higher for the PCSEL with RIT holes, and the net polarization of the vertically radiated beam is expected to be along the $\hat{x} + \hat{y}$ direction as well.

The customized PCSEL structure was grown by a commercial epitaxy supplier. A 150 nm SiN_x hard mask was deposited by plasma-enhanced chemical vapor deposition. The holes were patterned by electron beam lithography with a ~140 nm positive resist. The pattern was transferred from the resist to the SiN_x hard mask first, then further to GaN by a two-step dry-etching. The residual SiN_x was removed by immersion in buffered oxide etchant. The lateral dimension of the photonic crystal pattern is 250 μm. The photoluminescence (PL) spectrum was measured under a 355 nm pulsed laser with1 kHz repetition rate and 0.5 ns pulse width. The excitation beam was split with a 50/50 beam splitter; one path was directed to a power monitor, while the other was focused onto the sample surface from a tilted direction through a lens. The excitation spot diameter is estimated ~300 μm. The optical image and PL collection were via a 100× objective lens in the normal direction, and the PL was characterized with a high-resolution spectrometer (iHR-320, Horiba). Fig. 4(a) shows the PL spectra of the sample under sub-threshold and above-threshold excitation. The sub-threshold PL emission peak is located around 430 nm, corresponding to the spontaneous recombination from the QW. The broad PL spectrum is attributed to the simultaneous excitation of the p-GaN PhC slab and the InGaN waveguide layer. We designed and fabricated three sets of PCSELs with CC holes in different lattice constants: 167 nm, 170 nm, and 173 nm, with a constant FF of 0.11. The lasing wavelengths are 417.8 nm, 423.6 nm, and 428.8 nm, respectively. The normalized frequency is calculated to be 0.404, which is consistent with the simulated band edge in Fig. 1(d). The relationship between the lattice constant and the resonant wavelength confirms lasing in the photonic crystal band edge mode, and more likely, in B-mode due to its highest

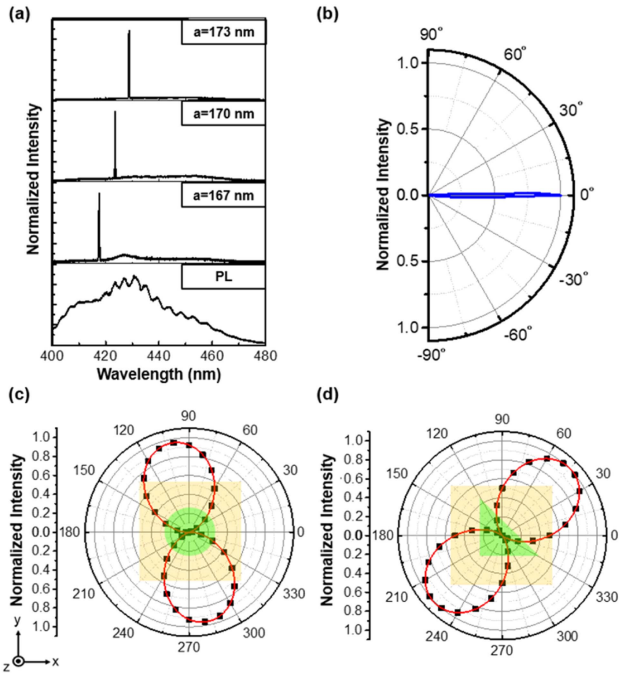

Fig. 4. (a). Emission wavelengths below and above the threshold with varying lattice constants with CC holes. (b) Normalized far-field intensity plot of a selected PCSEL from (a) Polarization characteristics for PCSELs with (c) CC and (d) RIT holes, respectively.

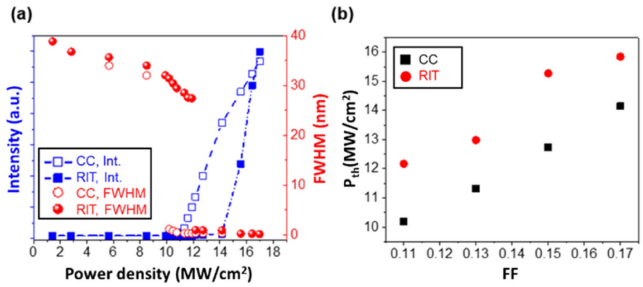

Fig. 5. (a). Light–light characteristics and FWHM spectra of PCSELs with CC and RIT air holes under varying pumping power densities. (b) Extracted lasing thresholds as a function of FF for both CC and RIT structures.

Q-factor. Fig. 4(b) shows the normalized angle-resolved far-field pattern slightly above the threshold from the a = 170 nm case in Fig. 4(a). The divergence angle is approximately 3.6°, indicating highly directional output. It's worth noticing that the samples are grown and measured on the single-side-polished wafers, and the coherent emission shall be coupled vertically in both directions. The actual divergence angle can be further reduced if the PCSEL is fabricated on a double-side polished bulk GaN substrate, while scattering from the backside can be further suppressed. Fig. 4(c) and 4(d) illustrate the far-field polarization characteristics of the sample with CC and RIT air holes after lasing, respectively. The one with CC holes exhibits linearly polarized emission, along the direction of ∼10° off the y-axis. Theoretically, PCSEL with CC holes shall out-couple a vectorial field with a vortex. [35], [36] The linearly polarized emission might be a result of the random pattern irregularities due to the unoptimized processing conditions. In contrast, the one with RIT holes exhibits a clear linear polarization along the $\hat{x} + \hat{y}$ direction, as the theoretical simulations predicted. This further suggested that the polarization of the PCSEL emission is more robust to processing with low-symmetry air holes.

Finally, we also fabricate PCSELs with a varying FF to verify our optical simulations. The lattice constant of each given FF is tuned to ensure all lasing wavelengths reside from 420 nm to 425 nm. Fig. 5(a) shows the representative light-light (L-L) curves with the full-width at half-maximum (FWHM) for both PCSELs with an FF of 10%. The blue solid and open squares represent the output intensities of PCSEL with CC and RIT air holes, respectively. The PCSEL with RIT air holes demonstrates a steeper slope above the threshold, which is consistent with the higher α_{rad} in Fig. 2(c) than that in Fig. 2(f). The FWHM values after lasing are approximately 1 nm for both structures. The peak threshold pumping power density (P_{th}) of PCSEL with CC holes is 10.2 MW/cm^2, while that with RIT holes is 12.2 MW/cm^2. It is worth noticing these numbers have not considered the power losses from the beam splitter to the focusing spot and the parasitic band-edge absorption from the top p-GaN layer yet. The relatively high threshold level is also partly attributed to that the epi is grown on the sapphire substrate and the single quantum well design. The P_{th} shall be significantly reduced if the active region structure can be further optimized on a high-quality GaN substrate. The CC configuration, consisting of highly symmetric circular holes arranged in a periodic lattice with C_{4v} symmetry, supports mode degeneracy at the Γ point. Such symmetry enables strong in-plane confinement and minimal out-of-plane radiation loss, leading to high Q factors and facilitating low-threshold lasing in Fig. 2(b) than that in Fig. 2(e). The RIT cavity incorporates geometrically asymmetric air holes to deliberately break the in-plane rotational symmetry, leading to the lifting of degeneracy between symmetric Bloch modes. This modal splitting enhances the coupling of the desired mode to free-space radiation while simultaneously suppressing unwanted competing modes, enabling robust single-mode operation. Such characteristics suggest that the RIT design, in spite of a slightly higher threshold, is advantageous for high-power applications due to its efficient far-field coupling and strong modal selectivity. We further measured the L-L-FWHM curves of PCSELs with an FF ranging from 0.11 to 0.17, and the extracted P_{th}'s on FF are plotted in Fig. 5(b). Both PCSELs exhibit the increasing P_{th} with the increasing FF, which is also consistent with what simulations have predicted.

III. Conclusion

In conclusion, we have demonstrated and compared two photonic crystal laser cavity designs, CC and RIT holes, regarding their lasing behavior, physics, and potential for applications. The CC structure benefits from its high rotational symmetry, which supports mode degeneracy and efficient in-plane confinement. This leads to a lower threshold due to minimized vertical radiation loss and a high cavity Q-factor. In contrast, the RIT structure introduces controlled geometric asymmetry to break rotational symmetry, which lifts the degeneracy of Bloch modes. The

resulting modal splitting enhances coupling of the target mode to the vertical direction and suppresses competing modes. While this leads to a higher threshold due to a lower Q-factor, the RIT cavity exhibits higher slope efficiency after the lasing threshold, indicating enhanced stimulated emission efficiency and better carrier-to-photon conversion. Furthermore, its far-field emission characteristics are favorable for power scaling applications and a robust polarization direction. The experimental results confirm that both CC and RIT PCSELs exhibit an increasing threshold with increasing FF, which is consistent with simulation results. These findings validate the effectiveness of symmetry engineering in PCSEL design and offer practical pathways toward wavelength-stable, high-efficiency surface-emitting lasers in the GaN regime.

REFERENCES

[1] M. De Zoysa et al., "Non-mechanical three-dimensional LiDAR system based on flash and beam-scanning dually modulated photonic crystal lasers," *Optica*, vol. 10, no. 2, pp. 264–268, 2023.

[2] M. Yoshida et al., "High-brightness scalable continuous-wave single-mode photonic-crystal laser," *Nature Commun.*, vol. 618, pp. 727–732, 2023.

[3] B. C. King et al., "Coherent power scaling in photonic crystal surface emitting laser arrays," *AIP Adv.*, vol. 11, no. 1, Jan. 2021, Art. no. 015017.

[4] R. J. E. Taylor et al., "Electronic control of coherence in a two-dimensional array of photonic crystal surface emitting lasers," *Sci. Rep.*, vol. 5, 2015, Art. no. 13203.

[5] L. R. Chen, K. B. Hong, H. L. Chen, K. C. Huang, and T. C. Lu, "Vertically integrated diffractive gratings on photonic crystal surface emitting lasers," *Sci. Rep.*, vol. 11, Mar. 2021, Art. no. 2427.

[6] H. Huang, C. Yang, H. Li, and Z. Zhang, "Unveiling the potential of photonic crystal surface emitting lasers: A concise review," *Semicond. Sci. Technol.*, vol. 40, no. 4, 2025, Art. no. 043001.

[7] Y. Itoh et al., "Power scalability of 1.55-μm-wavelength InP-based double-lattice photonic-crystal surface-emitting lasers with stable continuous-wave single-mode lasing," *IEEE J. Sel. Topics Quantum Electron.*, vol. 31, no. 2, 2024, Art. no. 1700408.

[8] Z. Wang et al., "Continuous-wave operation of 1550-nm low-threshold triple-lattice photonic-crystal surface-emitting lasers," *Light Sci. Appl.*, vol. 13, 2024, Art. no. 44.

[9] M. Kim et al., "1,550-nm photonic crystal surface-emitting laser diode fabricated by single deep air-hole etch," *Nanophotonics*, vol. 14, no. 4, pp. 515–522, 2025.

[10] T. Aoki et al., "High-power, stable single-mode CW operation of 1550 nm wavelength InP-based photonic-crystal surface-emitting lasers," *Appl. Phys. Exp.*, vol. 17, no. 4, 2024, Art. no. 042004.

[11] W. Zhou and M. Pan, "The future of photonic crystal surface-emitting lasers," *Appl. Phys. Lett.*, vol. 123, no. 14, 2023, Art. no. 140501.

[12] C. Gautam et al., "Laterally coupled photonic crystal surface emitting laser arrays," *J. Appl. Phys.*, vol. 135, 2024, Art. no. 193108.

[13] A. S. M. Kyaw et al., "Epitaxially regrown quantum dot photonic crystal surface emitting lasers," *Appl. Phys. Lett.*, vol. 123, 2023, Art. no. 140501.

[14] T. Inoue et al., "Comprehensive analysis of photonic-crystal surface-emitting lasers via time-dependent three-dimensional coupled-wave theory," *Phys. Rev. B*, vol. 99, 2019, Art. no. 035308.

[15] Z. Chen et al., "Analytical theory of finite-size photonic crystal slabs near the band edge," *Opt. Exp.*, vol. 30, no. 9, pp. 14033–14047, 2022.

[16] T. Inoue et al., "Towards optimization of photonic-crystal surface-emitting lasers via quantum annealing," *Opt. Exp.*, vol. 30, no. 24, pp. 43503–43512, 2022.

[17] Y. Wang et al., "Lateral cavity photonic crystal surface emitting laser based on commercial epitaxial wafer," *Opt. Exp.*, vol. 21, no. 7, pp. 8844–8855, 2013.

[18] J. J. Wierer Jr, A. David, and M. M. Megens, "III-nitride photonic-crystal light-emitting diodes with high extraction efficiency," *Nature Photon.*, vol. 3, pp. 163–169, 2009.

[19] S. W. Chen, T. C. Lu, and T. T. Kao, "Study of GaN-based photonic crystal surface-emitting lasers (PCSELs) with AlN/GaN distributed Bragg reflectors," *IEEE J. Sel. Topics Quantum Electron.*, vol. 15, no. 3, pp. 885–891, May/Jun. 2009.

[20] W.-H. Hsieh et al., "Optimal waveguide structure for low-threshold InGaN/GaN-based photonic-crystal surface-emitting lasers," *AIP Adv.*, vol. 14, no. 4, 2024, Art. no. 045108.

[21] D. Apaydın et al., "Deep-UV photonic crystal surface-emitting lasers," *Laser Photon. Rev.*, 2025, Art. no. e00271.

[22] K. Kusakabe, A. Kikuchi, and K. Kishino, "Characterization of overgrown GaN layers on nano-columns grown by RF-molecular beam epitaxy," *Jpn. J. Appl. Phys.*, vol. 40, pp. 192–194, 2001.

[23] J. Y. Lee et al., "Multiple epitaxial lateral overgrowth of GaN thin films using a patterned graphene mask by metal organic chemical vapor deposition," *J. Appl. Cryst.*, vol. 53, pp. 1502–1508, 2020.

[24] A. Kadys et al., "Epitaxial lateral overgrowth of GaN on a laser-patterned graphene mask," *Nanomaterials*, vol. 13, no. 4, 2023, Art. no. 784.

[25] J. Bin, K. Feng, W. Shen, M. Meng, and Q. Liu, "Investigation on GaN-based membrane photonic crystal surface emitting lasers," *Materials*, vol. 15, no. 4, 2022, Art. no. 1479.

[26] Q. Liu et al., "Design of GaN-based photonic crystal surface emitting lasers with top TiO_2 photonic crystals," *Materials*, vol. 33, Feb. 2022, Art. no. 105164.

[27] H. Matsubara et al., "GaN photonic-crystal surface-emitting laser at blue-violet wavelengths," *Science*, vol. 319, no. 5862, pp. 445–447, 2008.

[28] K. Emoto et al., "Wide-bandgap GaN-based watt-class photonic-crystal lasers," *Commun. Mater.*, vol. 3, 2022, Art. no. 72.

[29] S. Kawashima et al., "GaN-based surface-emitting laser with two-dimensional photonic crystal acting as distributed-feedback grating and optical cladding," *Appl. Phys. Lett.*, vol. 97, no. 25, 2010, Art. no. 251112.

[30] N. Taguchi et al., "Green-wavelength GaN-based photonic-crystal surface-emitting lasers," *Appl. Phys. Exp.*, vol. 17, 2024, Art. no. 012002.

[31] Y. Liang, C. Peng, K. Sakai, S. Iwahashi, and S. Noda, "Three-dimensional coupled-wave model for square-lattice photonic crystal lasers with transverse electric polarization: A general approach," *Phys. Rev. B*, vol. 84, 2011, Art. no. 195119.

[32] Y. Liang, C. Peng, K. Sakai, S. Iwahashi, and S. Noda, "Three-dimensional coupled-wave analysis for square-lattice photonic crystal surface emitting lasers with transverse-electric polarization: Finite-size effects," *Opt. Exp.*, vol. 20, no. 14, pp. 15945–15961, 2012.

[33] R. J. E. Taylor et al., "Mode control in photonic crystal surface emitting lasers through external reflection," *IEEE J. Sel. Topics Quantum Electron.*, vol. 23, no. 6, Nov./Dec. 2017, Art. no. 4900208.

[34] M. Imada, A. Chutinan, S. Noda, and M. Mochizuki, "Multidirectionally distributed feedback photonic crystal lasers," *Phys. Rev. B*, vol. 65, 2002, Art. no. 195306.

[35] S. Noda et al., "High-power and high-beam-quality photonic-crystal surface-emitting lasers: A tutorial," *Adv. Opt. Photon.*, vol. 15, no. 4, pp. 977–1032, 2023.

[36] C. J. Chang et al., "Dynamic control of topological charge of vector vortex in PCSELs with C_6 symmetry," *ACS Photon.*, vol. 10, no. 12, pp. 4112–4120, 2023.

Wen-Hsuan Hsieh is currently working toward the Ph.D. degree with the Department of Photonics, National Yang Ming Chiao Tung University, Hsinchu, Taiwan. He is currently a Member of the Advanced Nano Laser Laboratory and the Wide Bandgap Materials and Devices Laboratory. He has extensive experience in compound semiconductor design, waveguide simulation, process development, and establishment of measurement systems. His research interests include photonic crystal surface-emitting lasers and surface lattice resonance lasers, covering modeling, simulation, and fabrication, with several notable publications in these areas.

Kuo-Bin Hong received the M.S. and Ph.D. degrees from the Institute of Applied Mechanics, National Taiwan University, Taipei, Taiwan, in 2003 and 2010, respectively. His research interests include theoretical calculations of optical properties of quantum-dot-based semiconductor nanostructures, modeling and simulations of GaAs-based photonic crystal surface emitting lasers, GaN-based vertical cavity surface emitting lasers, surface-plasmonic nanolasers, and other optoelectronic devices.

Ching-Han Lin is currently working toward the graduation degree with the Department of Photonics at National Yang Ming Chiao Tung University, Hsinchu, Taiwan. His research focuses on the fabrication process development and device simulation of GaN-based photonic crystal surface-emitting lasers, with particular emphasis on optimizing device design.

Chen-Yu Yang is currently working toward the graduation degree with the Department of Photonics at National Yang Ming Chiao Tung University, Hsinchu, Taiwan. His research focuses on device simulation and characterization of GaN-based photonic crystal surface-emitting lasers, with particular emphasis on optimizing device design.

Tien-Chang Lu (Senior Member, IEEE) received the B.S. degree in electrical engineering from National Taiwan University, Taipei, Taiwan, in 1995, the M.S. degree in electrical engineering from the University of Southern California, Los Angeles, CA, USA, in 1998, and the Ph.D. degree in electrical engineering and computer science from National Chiao Tung University, Hsinchu, Taiwan, in 2004. From 2004 to 2005, he was with Union Optronics Corporation as the Manager of the Epitaxy Department. Since 2005, he has been a full-time Professor with National Chiao Tung University (now NYCU). He is currently a Chair Professor with the Department of Photonics, National Yang Ming Chiao Tung University, Hsinchu. He has authored or coauthored more than 200 journal papers. His research interests include the design, epitaxial growth, fabrication, and characterization of optoelectronic devices, with a focus on low-pressure MOCVD epitaxy, material processing, and device simulations. He was the recipient of the Pan Wen Yuan Foundation Exploration Research Award in 2007, Excellent Young Electronic Engineer Award in 2008, Young Optical Engineering Award (2010), the International Micro-Optics Conference Contribution Award (2011), the Dr. Ta-You Wu Memorial Award (2012), the Y. Z. Hsu Scientific Paper Award (2016), and the MOST Outstanding Research Award (2020, 2024). He has been an OSA Fellow since 2017 and an SPIE Fellow since 2021. He has served as Deputy Editor of the IEEE Journal of Lightwave Technology, and as an Associate Editor for the IEEE Journal of Quantum Electronics and Photonics journal.

Chia-Yen Huang (Associate Member, IEEE) received the B.S. degree in materials from National Taiwan University, Taipei, Taiwan, in 2007, and the Ph.D. degree in materials from the University of California, Santa Barbara, CA, USA, in 2012. During his Ph.D., he realized the world's first semipolar $(20\bar{2}\bar{1})$ laser diode under the supervision of Prof. Shuji Nakamura. After completing his doctoral degree, he worked in the Taiwanese LED industry for three years for the development of high-power blue LEDs. From 2015 to 2018, he was with the National Chiao Tung University (NCTU) as an Assistant Researcher focusing on new UV light sources. In 2018, he joined the Industrial Technology Research Institute (ITRI) to continue UVC LED epitaxy research with international industrial partners. In 2020, he demonstrated a technology breakthrough in strain-quality engineering of micrometer-thick AlGaN for high-power UVC LED technology. In 2021, he joined National Yang Ming Chiao Tung University (formerly NCTU) as an Assistant Professor, continuing research on wide bandgap materials and novel devices.